PHYSICAL REVIEW D **88,** 043011 (2013)

Linking electromagnetic and gravitational radiation in coalescing binary neutron stars

Carlos Palenzuela,[1] Luis Lehner,[2] Steven L. Liebling,[3] Marcelo Ponce,[4] Matthew Anderson,[5] David Neilsen,[6] and Patrick Motl[7]

[1]*Canadian Institute for Theoretical Astrophysics, Toronto, Ontario M5S 3H8, Canada*
[2]*Perimeter Institute for Theoretical Physics, Waterloo, Ontario N2L 2Y5, Canada*
[3]*Department of Physics, Long Island University, New York 11548, USA*
[4]*Department of Physics, University of Guelph, Guelph, Ontario N1G 2W1, Canada*
[5]*Pervasive Technology Institute, Indiana University, Bloomington, Indiana 47405, USA*
[6]*Department of Physics and Astronomy, Brigham Young University, Provo, Utah 84602, USA*
[7]*Department of Science, Mathematics and Informatics, Indiana University Kokomo, Kokomo, Indiana 46904, USA*

(Received 28 July 2013; published 26 August 2013)

We expand on our study of the gravitational and electromagnetic emissions from the late stage of an inspiraling neutron star binary as presented in Palenzuela *et al.* [Phys. Rev. Lett. **111**, 061105 (2013)]. Interactions between the stellar magnetospheres, driven by the extreme dynamics of the merger, can yield considerable outflows. We study the gravitational and electromagnetic waves produced during the inspiral and merger of a binary neutron star system using a full relativistic, resistive magnetohydrodynamics evolution code. We show that the interaction between the stellar magnetospheres extracts kinetic energy from the system and powers radiative Poynting flux and heat dissipation. These features depend strongly on the configuration of the initial stellar magnetic moments. Our results indicate that this power can strongly outshine pulsars in binaries and have a distinctive angular and time-dependent pattern. Our discussion provides more detail than Palenzuela *et al.*, showing clear evidence of the different effects taking place during the inspiral. Our simulations include a few milliseconds after the actual merger and study the dynamics of the magnetic fields during the formation of the hypermassive neutron star. We also briefly discuss the possibility of observing such emissions.

DOI: 10.1103/PhysRevD.88.043011 PACS numbers: 04.30.Db, 04.25.D−, 04.40.Nr

I. INTRODUCTION

Neutron stars are the most dense objects in the Universe; anything with higher density must collapse to a black hole. The neutron-rich matter in their cores is compressed to very high densities, where the equation of state, and hence their overall structure, is not completely understood. The strong gravitational fields of these stars lead to interesting relativistic effects, and their intrinsic magnetic fields are among the strongest arising in nature. Single neutron stars serve as the inner engine of pulsars and power exciting astrophysical events such as magnetar flares. Interactions of a neutron star with another neutron star or a black hole likely play a fundamental role in the production of gamma-ray bursts.

These compact binary systems are also among the most likely sources of detectable gravitational waves (GW). Understanding their behavior is important for gravitational wave astronomy enabled by advanced detectors such as Advanced LIGO/VIRGO. Gravitational wave observations of neutron star binaries are expected in the next few years, and the combination of these data with electromagnetic (EM) observations will provide new opportunities to study the fundamental physics associated with these stars. For example, such combined observations could reveal clues about their composition, test strong-field gravity, and provide stringent constraints on current models of their powerful electromagnetic emissions.

As an example of the important interplay between GW and EM data, consider the leading model of short, hard gamma ray bursts (SGRBs) (see e.g. [1] for a review). This model envisions a merging binary system of either two neutron stars or a neutron star and a black hole as the key ingredient to yield the energy and time scales observed in SGRBs. If the initial binary consists of two neutron stars, the merger may result in either the immediate collapse to a black hole or the creation of an intermediate, hypermassive neutron star, supported by thermal pressure and differential rotation, followed by a delayed collapse to a black hole. The interaction of the central compact object with a magnetic field can power radiation with the hard spectrum and short time scales characteristic of SGRBs.

Considerable effort has been devoted to understand possible scenarios to explain these bursts concentrating on emission after the merger. Recently however, there has also been significant interest in possible EM emissions preceding collapse. This interest has been motivated, in part, by both the desire to maximize opportunities for gravitational and electromagnetic wave detection, as well as surveys for EM transients that may be precursors to sGRBs (e.g. [2]) and other transients from compact binary mergers (e.g. [3,4]). Precursor emissions may be generated by crust cracking due to resonance effects [5] or magnetosphere interactions [6–10]. These studies rely on different approximations that may be adopted prior to the last

orbits of the system, when nonlinear interactions and dynamics do not overly complicate modeling possible emission mechanisms. It is in the final orbits, however, where nonlinear interactions are the strongest and the most powerful signals may be generated. As discussed recently in [11], for example, the dynamics of the magnetosphere around a collapsing hypermassive neutron star can induce significant electromagnetic output.

When studying EM emission from dynamic neutron star systems, it is crucial to properly model the dynamics of the global electromagnetic field, that is, incorporating in a consistent manner fields present in the stars as well as their effects in the magnetosphere region surrounding the compact objects (see discussion in [11]). We do so here considering general relativity coupled to relativistic, resistive magnetohydrodynamics (MHD) and study magnetized binary neutron stars, monitoring closely the radiation produced by the system.

In this work we concentrate on the late inspiral and merger epoch of a binary neutron star system and study possible electromagnetic and gravitational energy flux produced. Of particular interest is the localization of the dissipative regions and the analysis of the topology of the resulting electromagnetic field. We expand on previous work reported in [12].

This work is organized as follows. Section II describes details of our approach. We include in Sec. III a discussion of models presented to explain possible premerger emissions. In Sec. IV we describe results from numerical studies of three relevant systems, discuss their main features and compare the obtained behavior. We conclude in Sec. V with final comments and discussions.

II. APPROACH

Our primary goal is to investigate how the strongly gravitating and highly dynamical behavior of a binary neutron star system can affect the plasma in the magnetosphere such that powerful electromagnetic emissions can be induced. Such systems are natural candidates for loud gravitational wave emissions, and the interplay of strong/highly dynamical gravity with global electromagnetic fields should lead to bright electromagnetic signals. To study this problem we exploit a recently introduced framework incorporating general relativity and relativistic, resistive magnetohydrodynamics [13] (which builds from previous works [11,14,15]) to study the behavior of magnetically dominated plasma surrounding a binary magnetized neutron star system.

In this approach, the full Einstein-Maxwell-hydrodynamic equations are employed to model strongly gravitating compact stars and the effects of a global electromagnetic field. Inside the star, the magnetic field is modeled within the ideal MHD limit. The conductivity is prescribed so that the resistive scheme smoothly transitions from the ideal limit to the force-free limit outside the stars. This transition is achieved by setting the conductivity dependent on the fluid density, such that the conductivity varies by several orders of magnitude.

To incorporate gravitational effects in complete generality, we adopt a Baumgarte-Shapiro-Shibata-Nakamura formulation [16,17] of the Einstein equations as described in [18]. We use finite difference techniques on a regular, Cartesian grid to discretize the system [19,20]. The geometric fields are discretized with a fourth order accurate scheme satisfying the summation by parts rule, while high resolution shock capturing methods based on the Harten-Lax-van Leer-Einfeldt flux formulas with piecewise-parabolic-method reconstruction are used to discretize the fluid and the electromagnetic variables [21,22].

The time evolution of the resulting equations must address the appearance of certain stiff terms arising from the resistive MHD scheme in (some of) the equations of motion. Such terms are efficiently handled with an implicit-explicit (IMEX) Runge-Kutta scheme, as described in [13–15]. The explicit part of the time evolution is performed through the method of lines using a third order accurate Runge-Kutta integration scheme, which helps to ensure stability of the numerical implementation [14].

To ensure sufficient resolution in an efficient manner, we employ adaptive mesh refinement (AMR) via the HAD computational infrastructure that provides distributed, Berger-Oliger style AMR [23,24] with full subcycling in time, together with an improved treatment of artificial boundaries [25]. The refinement regions are determined using truncation error estimation provided by a shadow hierarchy [26] which adapts dynamically to ensure the estimated error is bounded within a prespecified tolerance.

III. PRELIMINARY LUMINOSITY ESTIMATES

The understanding of possible electromagnetic precursors driven by a compact binary system is an active area of research. In recent years several mechanisms have been discussed in this context, relying on simplified models, to obtain relevant estimates. A basic question here is what possible mechanisms could yield sufficiently strong electromagnetic emissions to be detected by different facilities (in suitable bands). Moreover, such detection might be further aided by gravitational wave input which in future years will provide timing and sky localization (in addition to other physical parameters). The information provided by future GW observations may also lead to deeper and longer investigations of signals on both fronts (e.g. [3,27–29]).

For the particular case of precursor signals from binary mergers the challenge is to identify appropriate mechanisms that could act prior to the stars coming into contact and yield significant (i.e., possibly observable) emissions. A few mechanisms have been recently discussed. One of these is the emission of flares induced by *resonant excitations of neutron star (NS) modes by tides*, which could induce crust cracking [5] and the consequent release of

10^{46-47} ergs of energy a few seconds before merger. Another relies on *unipolar induction*, which bears direct relevance to our present discussion and, for this reason, is discussed in some detail next. (A related model [30] examines possible emissions through Fermi acceleration at shocks created by Poynting flux-driven bubbles.)

The main mechanism in the unipolar inductor model is the extraction of stellar kinetic energy by the interaction of the stellar magnetosphere with an external magnetic field. In this case, one can consider each star to be interacting with the field of its companion. The energy released will either reach its maximum just prior to merger or give rise to episodic emissions depending on the resistance of an assumed "effective" circuit from one star to the other. Different models build upon this possibility [6–8], predicting a transient preceding the merger by (of order of) a few seconds, possibly accompanied by a radio signal.

A good starting point for this discussion is the model considered by Ref. [7]: a binary system with a magnetized primary star and an unmagnetized secondary. An estimate of the luminosity for such a configuration is given by

$$\mathcal{L} \approx \xi_\phi v_{\rm rel} \frac{B_*^2 R_*^6 R_c^2}{2a^6} \tag{1}$$

$$\approx 10^{41} \xi_\phi \left(\frac{B_*}{10^{11}\,{\rm G}}\right)^2 \left(\frac{R_c}{13.6\,{\rm km}}\right)^2 \left(\frac{a}{30\,{\rm km}}\right)^{-13/2} {\rm ergs/s} \tag{2}$$

where $\xi_\phi = 16 v_{\rm rel} R_{\rm tot}$ is the azimuthal twist of flux tubes connecting both stars; $v_{\rm rel}$ is the relative velocity; $R_{\rm tot}$ is the total resistance of the circuit; B_*, R_* are the field strength and radius of the primary star; B_c, R_c the field strength (assumed much weaker) and radius of the companion star; and a is the orbital separation [notice that to obtain Eq. (2) we assume values $R_* = R_c = 13.6$ km and $M_* = M_c = 1.4 M_\odot$]. A key unknown here is the azimuthal twist which depends on the total resistance. This resistance, in turn, depends on the conductivity of the stars and on the properties of the magnetosphere in between them. In the case of free space, $R_{\rm tot} = 4\pi$ and with this choice the luminosity becomes [7,8]

$$\mathcal{L} \approx 3 \times 10^{40} \left(\frac{B_*}{10^{11}\,{\rm G}}\right)^2 \left(\frac{R_c}{13.6\,{\rm km}}\right)^2 \left(\frac{a}{30\,{\rm km}}\right)^{-7} {\rm ergs/s} \tag{3}$$

which can be reexpressed in terms of the orbital frequency Ω (assuming a Keplerian relation) as

$$\mathcal{L} \approx 10^{41} \left(\frac{B_*}{10^{11}\,{\rm G}}\right)^2 \left(\frac{\Omega}{\Omega_{\rm ISCO}}\right)^{14/3} {\rm ergs/s} \tag{4}$$

in terms of the fiducial angular frequency $\Omega_{\rm ISCO} = 4758$ rad/s chosen to be that of a particle at the innermost, stable, circular orbit for a nonspinning black hole of mass $2.9 M_\odot$ (this frequency is a good mark of the onset of the plunging behavior [31,32]). Notice this luminosity is well below the saturation point of plasma acceleration, which happens when the plasma energy density becomes comparable to the energy density of the magnetic field companion [9]; thus the magnetosphere remains present.

The above estimate treats this problem as essentially a quasiadiabatic process with only one star dominating the magnetic effects, so that the induced circuit can be analyzed in simple terms. However more complex behavior arises when both stars are magnetized. For instance, already at the quasiadiabatic level when the companion is weakly magnetized, the radius at which induction occurs is not R_c but instead an effective radius that depends, at least, on the relative magnetizations of the stars.

For instance, in the simplest case of aligned dipolar fields the companion's field will shield the effects of the primary at some effective radius, $R_{\rm eff}$. We can estimate this radius by assuming equality of the magnetic field produced by each star at that location in terms of their magnetic moments

$$\mu_*(a - R_{\rm eff})^3 = \mu_c R_{\rm eff}^3 \tag{5}$$

where μ_* is the moment of the primary and μ_c is the moment of the companion. Because each star is essentially perfectly conducting with frozen magnetic flux in its interior, we have a lower bound $R_{\rm eff} \geq R_c$. Assuming $a \gg R_{\rm eff}$, $B_c \propto \mu_c$ and $B_* \propto \mu_*$, we then have

$$R_{\rm eff} = \max\left(a\left(\frac{B_c}{B_*}\right)^{1/3}, R_c\right). \tag{6}$$

The luminosity of Eq. (3) with $R_{\rm eff} \propto (B_c/B_*)^{1/3}$ yields

$$\mathcal{L} \sim 1.5 \times 10^{41} \left(\frac{B_*}{10^{11}\,{\rm G}}\right)^2 \left(\frac{B_c}{B_*}\right)^{2/3} \left(\frac{a}{30\ {\rm km}}\right)^{-5} {\rm ergs/s} \tag{7}$$

or, in terms of the orbital frequency,

$$\mathcal{L} \sim 2 \times 10^{41} \left(\frac{B_*}{10^{11}\,{\rm G}}\right)^2 \left(\frac{B_c}{B_*}\right)^{2/3} \left(\frac{\Omega}{\Omega_{\rm ISCO}}\right)^{10/3} {\rm ergs/s}. \tag{8}$$

This estimate already indicates that the relative magnetization of the stars introduces departures from the basic unipolar result of Eq. (3). One naturally expects further departures due to the dynamics of the magnetospheres; in particular, significant reconnections of the magnetic field lines may be induced which would depend on the orientation of the magnetic moments. In addition, as the stars approach merger, the increasing strength of the gravitational potential, the rapidly changing geometry of the spacetime, and the stellar dynamics will all affect the magnetic field. Naturally, estimating these effects is difficult, at best. Instead, we proceed with numerical solutions to unravel the possible phenomenology.

IV. BINARY NEUTRON STAR SIMULATIONS

We consider the late orbiting behavior and merger of magnetized binary neutron star systems. The magnetic field dynamics within the stars and the gravitational wave output from these systems have previously been studied through numerical simulations [33–36].

Our primary goal here is to understand magnetic effects arising in the magnetosphere and the dependence of these effects upon the initial magnetic configurations of the stars. Because tidal effects play a relatively minor role (and only close to the merger epoch) [37,38], and because electromagnetic interactions do not influence the dynamics of the binary for realistic field strengths [39], our studies are readily applicable to generic binary systems. For simplicity, we concentrate on a binary initially described by a pair of identical, irrotational neutron stars in a quasicircular orbit with an initial separation $a = 45$ km, $\Omega_o = 1.85$ rad/ms.

The initial geometric and matter configurations for this system are obtained with the LORENE library [40], which adopts a polytropic equation of state $P = K\rho^{\Gamma}$ with $\Gamma = 2$ and $K = 123$, approximating cold nuclear matter. During the evolution, the fluid is modeled as a magnetized perfect fluid with an ideal gas equation of state that allows for shocks. Note that the dynamics and interactions of the electromagnetic (e.g. [7,33,39]) and gravitational (e.g. [32,37]) fields are largely insensitive to the choice of equation of state during the inspiral.

For convenience, unless otherwise noted, we adopt geometrized units $G = c = 1$, such that all quantities, including mass (M) and time (T) have units of length (L). Additionally we set the solar mass $M_{\odot} \equiv 1$. The above choice then constitutes our "code units," and the relation between code and physical length units is given by the multiplicative factor 1.48 km. Unless otherwise noted by their appropriate physical units, we will be displaying code units in our figures.

We adopt individual stars having a baryonic mass $M = 1.62M_{\odot}$, radius $R_* = 13.6$ km, and a magnetic moment μ_i that describes a dipolar magnetic field B^i in the comoving frame of each star. The magnetic moment is aligned with the orbital angular momentum, i.e. $\mu_i = (0, 0, \mu)$. The nontrivial component is related to the radial magnetic field at the pole of the star, B_*, by the relation $\mu = B_* R_*^3$. In our simulations we choose $B_* = 1.5 \times 10^{11}$ G, a value which is relatively high for neutron stars in binaries but still realistic. The electric field is obtained from the ideal MHD condition $\mathbf{E} = -\mathbf{v} \times \mathbf{B}$, where the velocity in the star is given by the orbital motion and we assume that the magnetosphere is initially at rest.

To cover the range of possible cases and to gain insight into the underlying behavior, we consider three different initial configurations of magnetic moments of each star (i):

(i) U/U: aligned case $\mu_{(1)} = \mu_{(2)} = \mu$,
(ii) U/D: antialigned case $\mu_{(1)} = -\mu_{(2)} = \mu$,
(iii) U/u: one-dominant, aligned case $\mu_{(1)} = 100\mu_{(2)} = \mu$.

Notice that the last case (U/u) has magnetic moments similar to those estimated in the double binary pulsar PSR J0737-3039 [41], and the orientation of the moments resembles one of two configurations obtained in a model of that same system [42]. Future work will explore configurations with other inclinations of the magnetic moments with respect to the orbital angular momentum.

Our numerical domain extends up to $L = 320$ km and contains five, centered fixed-mesh-refinement grids with decreasing side lengths (and twice as well resolved) such that the highest resolution grid has $\Delta x = 300$ m and extends up to 58 km, covering both stars and the inner part of the magnetosphere. We have computed the Poynting-vector luminosity at three different surfaces, the furthest located at $R_{\rm ext} = 180$ km. Within this setup, we have evolved the three cases described above and have studied the resulting behavior. We have also compared coarser solutions obtained for the U/U and U/D cases and have found that the qualitative features of the magnetic fields are very similar and that the luminosity differs only by a few percent. Our main results are summarized in the following sections.

A. Orbital motion and gravitational waves

In all cases, the field strengths considered have a negligible effect in the orbital dynamics of the system up to the merger [33,39]. Consequently, the three cases studied progress to merger in exactly the same way, producing the same gravitational signal.

Figure 1 illustrates the path of the stars by displaying the location of the maximum of the fluid densities. The stars orbit about each other for ≈ 2.5 orbits before they come into contact. Figure 2 displays the gravitational signal, represented by the $l = 2$, $m = 2$ (the most dominant) component of $rM_{\rm total}\Psi_4$ (for a representative analysis of the late inspiral GW from this binary see e.g. [32]). This signal displays the standard "chirping" behavior in which the amplitude and frequency grow as the orbit shrinks due to the radiation of angular momentum via gravitational waves. The merger of these stars produces a hypermassive, differentially rotating neutron star which emits gravitational

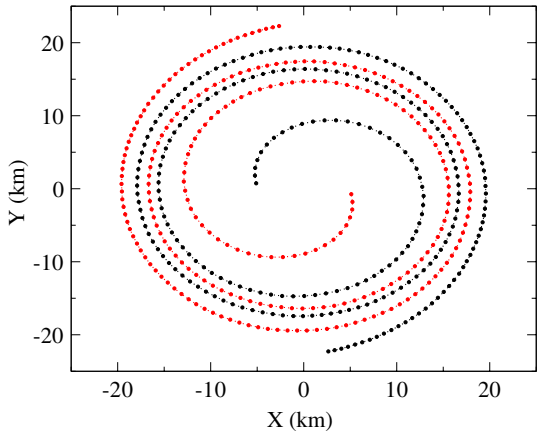

FIG. 1 (color online). Trajectory of the binary as measured by the location of the maximum densities as functions of time. The system undergoes about 2.5 orbits before the stars come into contact.

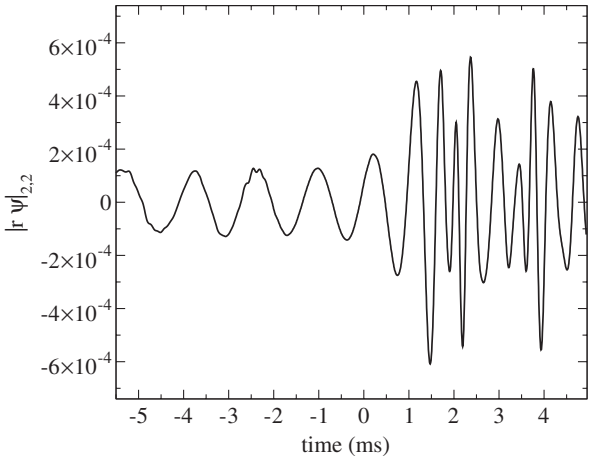

FIG. 2. The dominant $l = m = 2$ mode of the gravitational wave extracted at $R_{\rm ext} = 180$ km. The time $t = 0$ is set as the moment when the stars first make contact.

waves as it radiates excess energy and angular momentum before succumbing to collapse to a black hole.

As a result of the merger, as discussed in [33,43,44], magnetic fields can be amplified—via diverse mechanisms such as winding, Kevin-Helmholtz and MRI instabilities—to values large enough that magnetic effects can indeed affect the *postmerger* dynamics, and thus the corresponding gravitational wave signatures. To accurately resolve such effects, resolutions at least an order of magnitude better are required. Furthermore, differences in the postmerger dynamics can arise from the choice of equation of state which also impacts the waveform characteristics. We therefore focus our analysis primarily up to the merger stage and discuss briefly the early postmerger epoch, leaving for future work a closer examination of this late stage. We note however, as discussed in [11,13], that late-stage collapse can induce significant electromagnetic emission.

B. Electromagnetic radiation and dissipation

In spite of the orbiting behavior being the same for all three cases considered, the electromagnetic field dynamics and magnetosphere interactions naturally depend sensitively on the orientation of the magnetic dipole moments of the stars. Such interactions strongly affect the resulting topology of the global electromagnetic field and may induce dissipation regions, reconnections of field lines, and a net Poynting flux, as well as several other relevant features. At a rudimentary level, the accelerated orbital motion of the stars induces only a small degree of winding of its magnetic field lines; thus the magnetospheres essentially corotate with the stars and the magnetic field at their surfaces (and therefore, the magnetic dipole moments) remains almost constant until the merger. For the sake of clarity, we first discuss the main features of each case separately and then compare and contrast particular aspects among the three cases. Henceforth we set $t = 0$ as the time at which the stars touch.

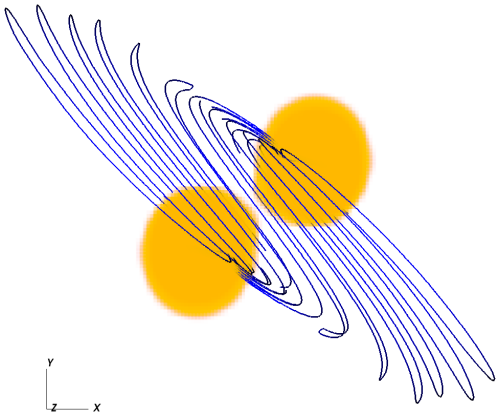

FIG. 3 (color online). U/D case. Top-down view of certain magnetic field lines along with the stellar density at $t = -1.7$ ms. Only field lines originating along a line connecting the stars slightly above the equatorial plane are shown for clarity. Similar plots for the other cases are shown in Fig. 6 (U/U) and Fig. 9 (U/u). Note that reconnections near the leading edges of the stars (orbiting counterclockwise in this view) have severed some lines which would otherwise connect the stars.

1. U/D case

Figure 3 illustrates the behavior of the antialigned case (U/D) in which both stars have equal magnitude magnetic moments but opposite directions—with individual directions parallel and antiparallel to the orbital angular momentum. The corotation of the magnetospheres with the stars induces a shear layer in the midplane, separating two regions filled with magnetically dominated plasma moving in opposite directions. The poloidal component of the magnetic field from each star switches direction as one crosses the midplane, allowing for reconnections that result in field lines connecting both stars. The projection of these connecting field lines are quite apparent in Fig. 4.

As the stars orbit, these field lines are severely stretched, increasing their tension and developing a strong toroidal component. Near the leading edge of each stellar surface, these field lines undergo a twisting so extreme that they are bent almost completely backwards, allowing them to reconnect and release some of the orbital energy stored by the twisted magnetic fields. A careful examination of both Figs. 3 and 4 provides a view of S-shaped toroidal field lines connecting the stars. The sense of the "S" changes as one crosses below the equatorial plane as shown in Fig. 4. As the stars orbit, our view of the S shape changes so that the colors switch with each half-orbit.

The region near the stars, and especially near the orbital plane, is much more complicated. Reconnections at the midplane produce a current sheet that propagates outwards, forming a spiral pattern. The current sheet structure is shown in Fig. 5, and it rotates with the periodicity of the orbital motion, Assuming that the current sheet would produce electromagnetic radiation, then this structure may effectively provide a "spacetime tracer" of the orbital motion.

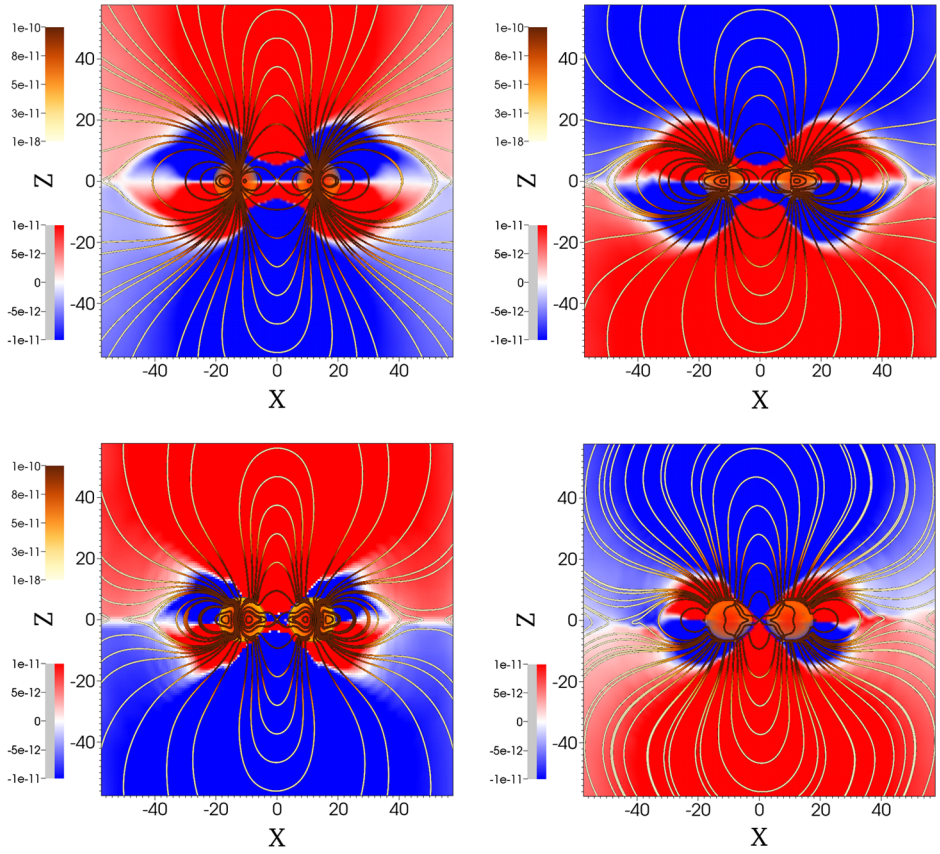

FIG. 4 (color online). U/D case. Snapshots of the magnetic field configuration on the $y = 0$ plane at half-orbital periods (times $t = -4.6, -3.2, -1.7$ and -0.5 ms). Poloidal field lines are shown while the component perpendicular to the plane (related to the toroidal component) is shaded in color. Similar plots for the other cases are shown in Fig. 7 (U/U) and Fig. 10 (U/u). The field lines connecting the stars result from reconnection. Note that after each half-orbit, the direction of the perpendicular component switches direction due to the change in sign of the poloidal field.

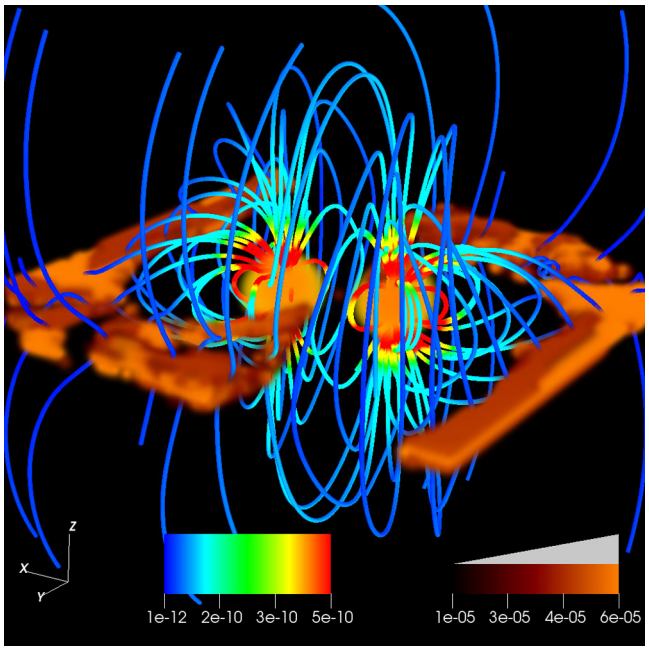

FIG. 5 (color online). U/D case. Representative snapshot of the magnetic field configuration and induced current sheet at $t = -2.9$ ms.

The dynamics also impact the distribution of charges and currents as illustrated in Fig. 12. The top panel of this figure shows the currents of the U/D case with arrows. A circuit is established, with current flowing from the star on the left to the one on the right well above and below the equator, with a returning current closer to the equator. These currents become stronger as the stars get closer.

2. U/U case

We turn now to general features displayed by the aligned (U/U) case in which both stars have identical magnetic moments, parallel to the orbital angular momentum. A sense of the magnetic field structure for this case is given by Fig. 6. Similar to the U/D case, a shear layer in the midplane between the stars arises due to the oppositely directed velocities of the magnetospheres. However, unlike the U/D case, the magnetic fields on both sides of the shear layer generally point in the same direction and therefore do not reconnect.

Again, rotation induces a toroidal magnetic field although the topology is clearly different than the one observed in the U/D case. Here, the deflection of the field lines from each star at the midplane produces a strong,

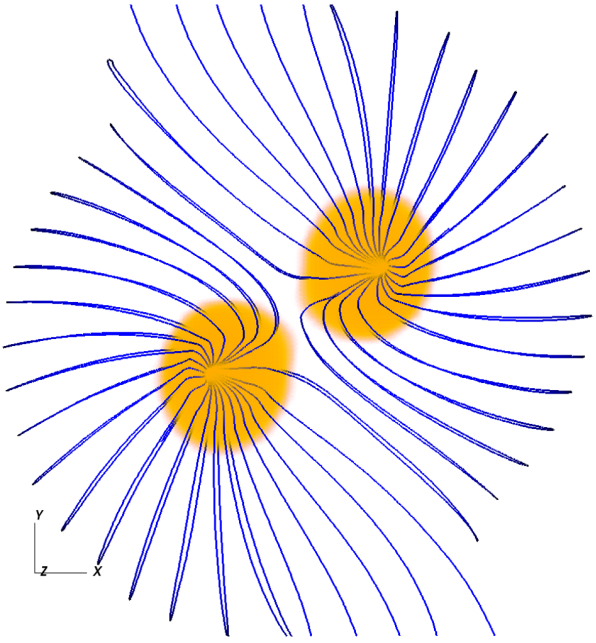

FIG. 6 (color online). U/U case. Top-down view of certain magnetic field lines along with the stellar density at $t = -1.7$ ms. Similar plots for the other cases are shown in Fig. 3 (U/D) and Fig. 9 (U/u). The repulsion of roughly aligned field lines is clearly visible at the midplane between the stars.

antisymmetric toroidal component in the central region of the midplane. Far from the stars, the structure is reminiscent of the one obtained in the aligned (dipole) rotator (see e.g. [13,45,46]). One aspect of this rotator structure is the appearance of a Y point in the poloidal field along the equatorial plane roughly at large radius [see the points near ($\pm$ 45, 0)] in the last panel of Fig. 7). This point separates closed from open field lines and occurs at the *light cylinder*, the radius $R_{\rm LC} = c/\Omega$ at which the velocity of the corotating magnetosphere reaches light speed. Another aspect similar to the rotator is oppositely directed toroidal field as one cross the equatorial plane. This structure is natural, as there is a net effective dipole to leading order in the system. However in this case the symmetry of the system implies an (approximate) periodicity in the solution given by half the orbital period, which is more evident in Fig. 7.

Furthermore, a current sheet is induced on the equatorial plane as shown in Fig. 8. The current sheet first arises at the light cylinder which shrinks as the orbit tightens, resembling that of an aligned rotator. Once again the current sheet reflects the dynamics of the binary and hence may be a tracer of the spacetime. In particular, the current sheet is not homogeneous along the azimuthal direction, presenting a spiral pattern. The induced current distribution and charge density are displayed in the middle panel of

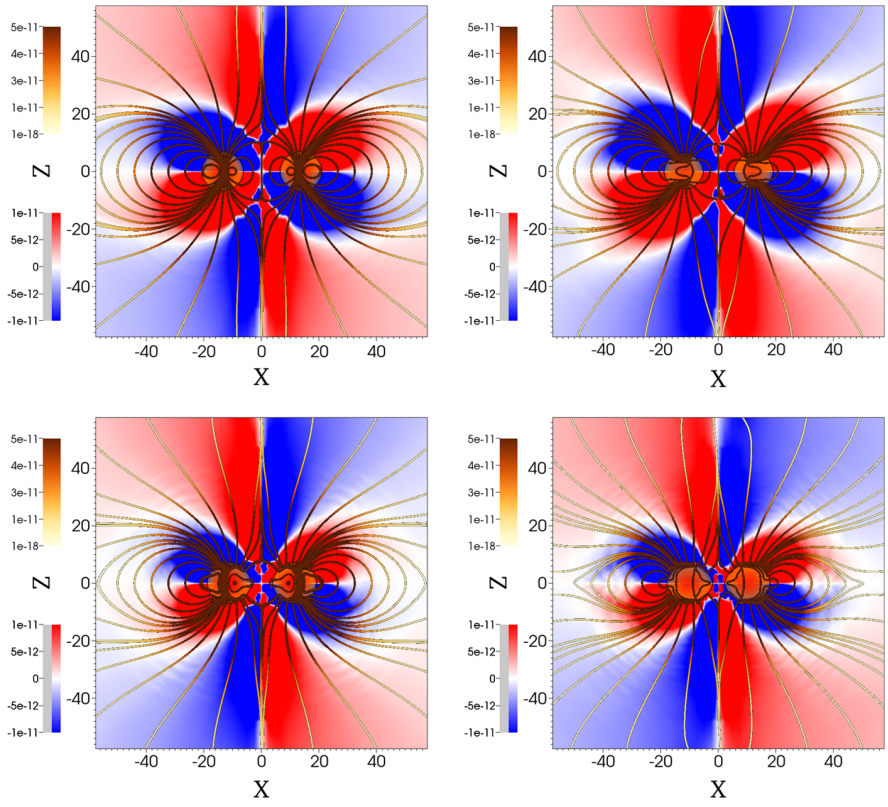

FIG. 7 (color online). U/U case. Snapshots of the magnetic field configuration on the $y = 0$ plane at half-orbital periods (times $t = -4.6, -3.2, -1.7$ and -0.5 ms). Similar plots for the other cases are shown in Fig. 4 (U/D) and Fig. 10 (U/u). Note that field lines near the midplane repel each other as is more evident in Fig. 6. Far from the binary at large radii, the magnetic field structure resembles that of an aligned rotator. Indeed the direction of the magnetic field changes across the equatorial plane and a Y point arises as the orbit tightens.

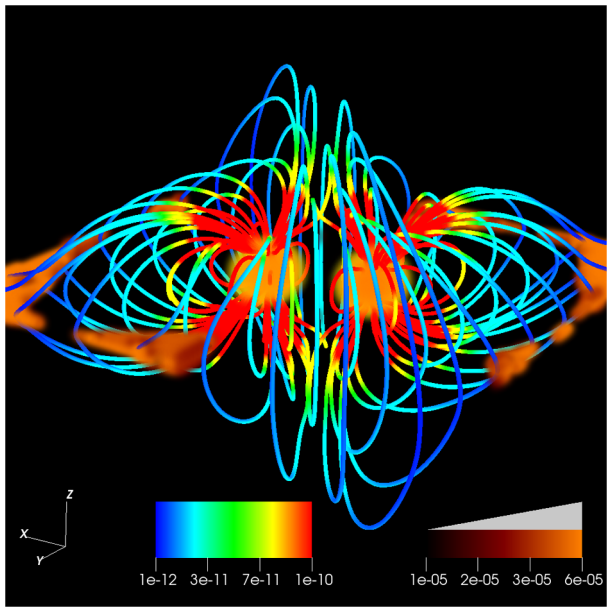

FIG. 8 (color online). U/U case. Snapshot of the magnetic field configuration and induced current sheet at $t = -2.9$ ms.

Fig. 12, revealing a strong current along the z axis towards the center surrounded by a sheath of outwardly directed current.

3. U/u case

The last of the three cases, U/u, contains one star significantly less magnetized (just 1%) than the other, although both moments are initially aligned. Among these cases, this U/u case most resembles the models of [6–8] which study a binary with just one star initially magnetized. These models invoke the unipolar inductor as discussed earlier in Sec. III. As mentioned there, when the stars are well separated, the field produced by the weaker star shields the star from the more magnetized field within some effective radius. Figure 9 illustrates that the magnetic field from the strongly magnetized star eventually dominates that of the companion. As a consequence, the global electromagnetic field for the system is roughly described by an inspiraling, magnetic dipole perturbed by induction effects on the weaker star.

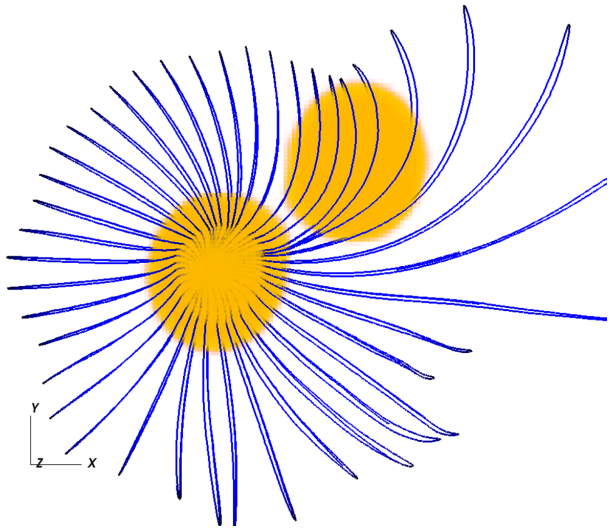

FIG. 9 (color online). U/u case. Top-down view of certain magnetic field lines along with the stellar density at $t = -1.7$ ms. Similar plots for the other cases are shown in Fig. 3 (U/D) and Fig. 6 (U/U). Note that field lines emanating from the strongly magnetized star bend both around the weaker star and the region just in front of it (the stars are orbiting counterclockwise). Similarly, the lines behind the weaker star are distorted by a trailing current sheet.

The magnetic field for the U/u case is also shown in Fig. 10. Note that in the first panel, one can see that the weaker field shields the less magnetized star (on the right) from that of the dominant star.

An interesting effect occurs as magnetic field lines originating from the strongly magnetized star slide off the companion's surface and then reconnect. This reconnection produces a trailing region of dissipation, quite visible in Fig. 11. The extent of this dissipative tail gradually grows as the stars orbit, populating a current sheet.

The induced current and charge density reveal a structure consistent with the unipolar induction model, as can be seen in the bottom panel of Fig. 12. A closed circuit between the stars is shown, with current flowing along the magnetic field lines from the strongly magnetized star to the rear of the weakly magnetized one. This current makes its return along the stellar surface until it follows the returning field lines back to the strongly magnetized star to complete the circuit (see for instance the diagram in Fig. 1 of [7]).

C. Poynting flux and energy dissipation

Of particular interest is the electromagnetic radiation from these configurations. To assess their radiative properties, we study the outward Poynting flux and find it significant (we discuss their potential observability in Sec. V) with noticeable differences among the three cases. We show two different views of the Poynting flux for each case in Fig. 13. On the left, a volume rendering shows the flux outside the stars. On the right, this flux is evaluated on a binary-centered spherical surface at a radius $r = 80$ km. As evident in the figure, both the U/D and U/U cases radiate strongly along the shear layer between the two stars while the U/u case does so mainly near the equatorial plane and primarily in the direction of the strongly magnetized star.

The radiation in the U/D and U/U cases is partially collimated. Notice that, since the Poynting flux is symmetric across the equator ($\theta_\circ \to \theta_\circ + 90°$) for the configurations considered here, it is sufficient to describe only the northern hemisphere. The U/D case has a flux density in a polar cone (with opening angle of $\theta_\circ < 30°$) which is 2.5

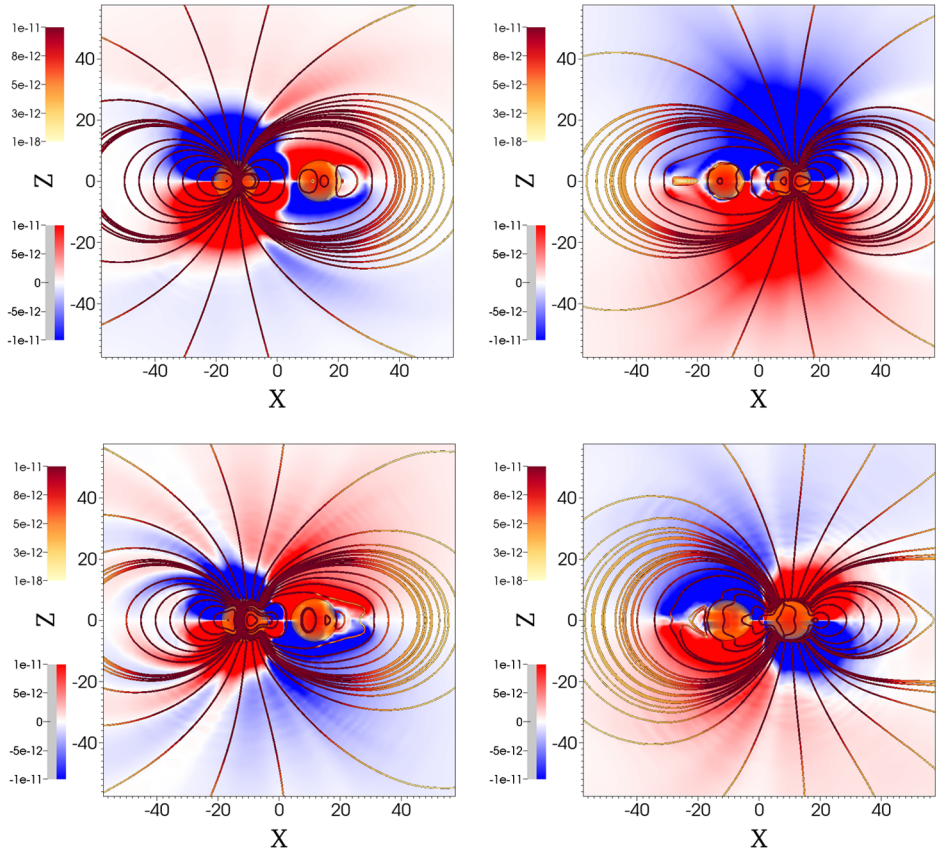

FIG. 10 (color online). U/u case. Snapshots of the magnetic field configuration on the $y = 0$ plane at half-orbital periods (times $t = -4.6, -2.9, -1.7$ and -0.5 ms). Similar plots for the other cases are shown in Fig. 4 (U/D) and Fig. 7 (U/U). Notice that the magnetic field structure is mainly described by an orbiting dipole perturbed by the interaction with the weakly magnetized companion and its trailing current sheet.

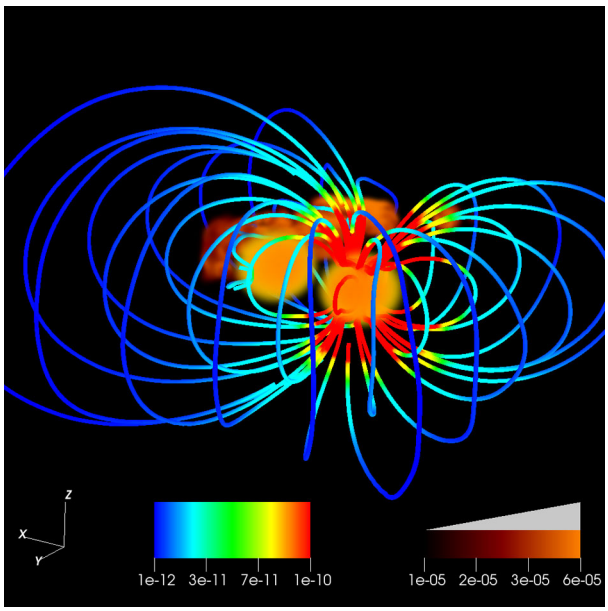

FIG. 11 (color online). U/u case. Snapshot of the magnetic field configuration and current sheet at $t = -1.7$ ms.

times larger than the average and accounts for $1/3$ of the total radiated energy. The U/U case radiates in this polar cone about 1.9 times larger than its average luminosity and represents $1/4$ of the total power. The radiation from the U/u case is emitted mainly near the equatorial plane, with $2/3$ of the total energy radiated between $60° < \theta_{\circ} < 90°$. Besides the difference in angular distribution, Fig. 13 indicates that the peak U/u flux is roughly a tenth that of the other two cases. More quantitatively, we integrate the flux and display the total Poynting luminosity for each case in Fig. 14 (solid lines). The behavior of these luminosities in time can be characterized in terms of powers of the orbital frequency of the binary as a function of time, such that $L \propto \Omega^p$ (assuming a constant surface magnetic field). We include on the graph a few curves for different values of p suggested by the data.

At early times, the luminosity of the U/u case increases roughly as $\Omega^{14/3}$, which is consistent with the unipolar inductor [see Eq. (4)]. In contrast, the behavior of both the U/U and U/D cases differs from the $\Omega^{10/3}$ expectation of the unipolar inductor as modified for both stars being magnetized [see Eq. (8)]. Instead, their luminosities increase

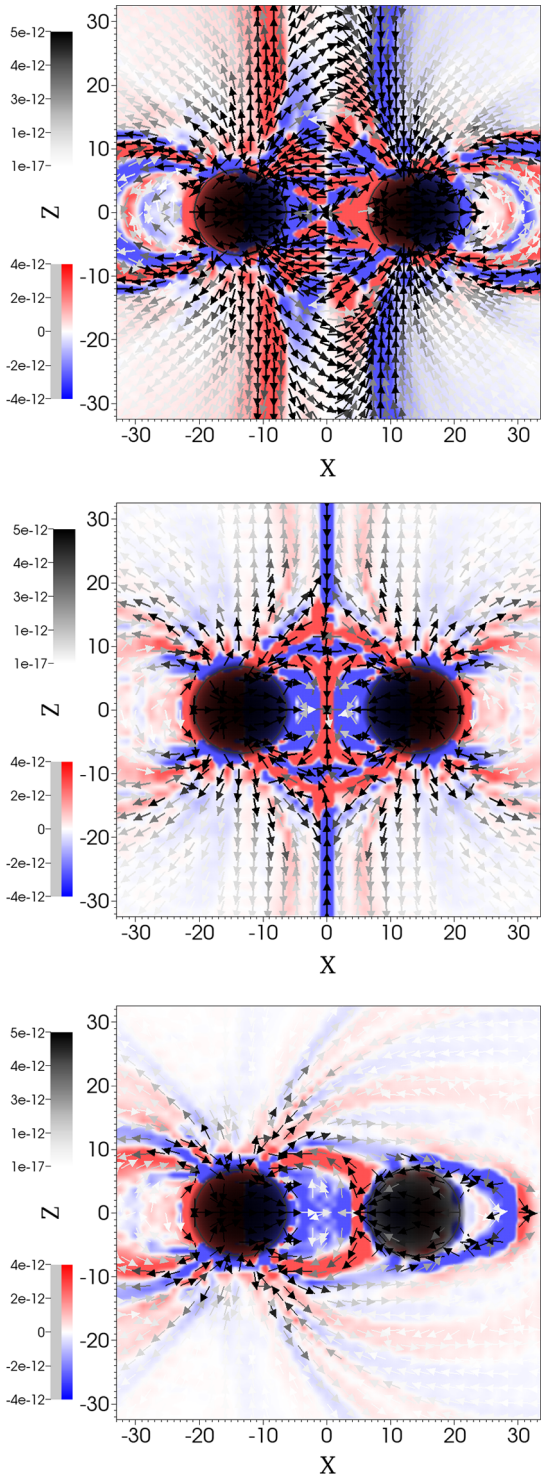

FIG. 12 (color online). Currents (drawn as arrows) and charge density (color coded) for the U/D (first panel), U/U (second panel) and U/u (third panel) case at $t = -4.6$ ms. In all cases an effective circuit arises; however the circuits extend significantly in both vertical directions for the first two cases which contrasts with the more localized circuit in the last case. The bottom panel resembles the diagram in Fig. 1 of [7].

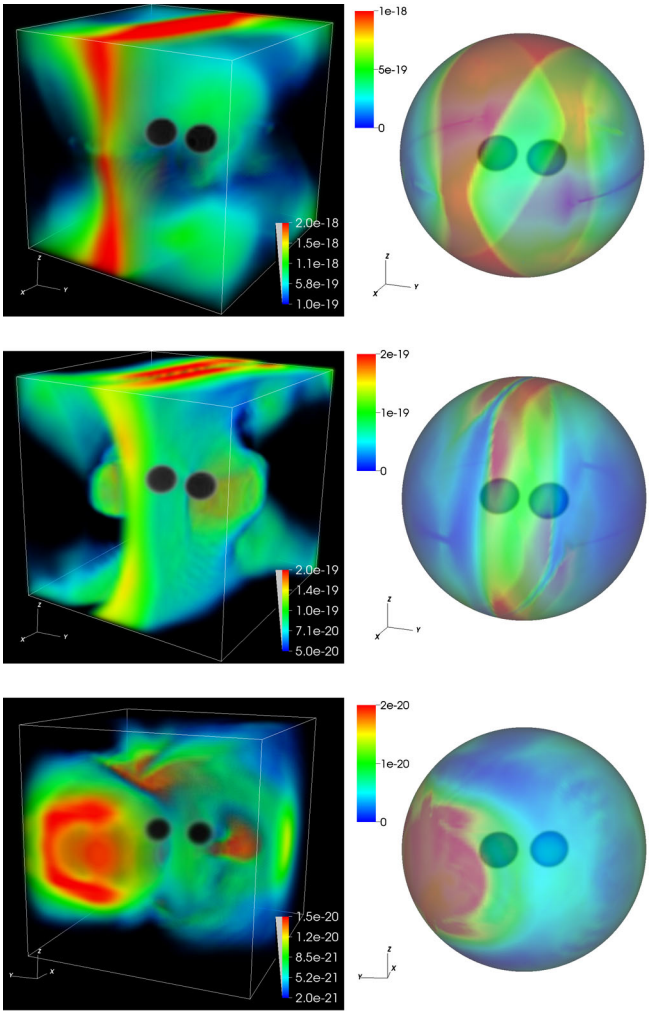

FIG. 13 (color online). Poynting flux as a volume rendering (left) and evaluated on an encompassing sphere (right) at $t = -2.9$ ms. The U/D case (top row), the U/U case (middle row) and the U/u (bottom row) cases are shown. The sphere is located at a radius $r = 80$ km. The top two cases radiate more strongly away from the equatorial plane than that of the U/u case. The U/u case radiates quite asymmetrically in the direction of the more magnetized star and mostly near the orbital plane.

with $p \simeq 1$–2 until the stars come into contact. Interestingly all three cases transition to much more rapid growth ($p \approx 12$) at later times (the U/u case begins this growth a bit earlier than the other two cases). The agreement of the slopes near merger ($t \approx 0$) for all the cases suggests that the dynamics near merger are dominated by the formation of the hypermassive neutron star, independent of the initial magnetic configuration.

This plot also highlights several other important details. First, the U/D case is significantly more radiative than the U/U case. This disparity is interesting as the "inner engine" in both cases consists of the magnetic dipole of each star and their respective orbital motion, which are the same except for the direction of the dipoles. The different

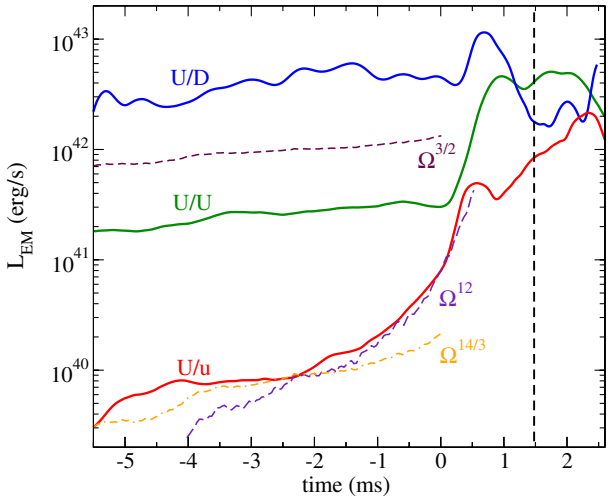

FIG. 14 (color online). Electromagnetic luminosity for the three different magnetic field configurations. Additionally, three curves illustrating $L \propto \Omega^p$ with $p = \{3/2, 14/3, 12\}$ are shown as guidance. The maximum of the gravitational radiation, marked with a vertical dashed line, occurs approximately at $t \approx 1.48$ ms.

luminosities therefore imply a more efficient tapping of orbital energy with antialigned magnetic moments (U/D) than when they are aligned (U/U), possibly due to the additional energy radiated by the release of magnetic tension in the U/D case through reconnections near the stars. We have monitored that the electromagnetic energy in the interior of the stars remains essentially constant during the inspiral, with a sudden increase when the star surfaces touch.

Of course, as the stars merge the shear between them will considerably increase the magnetic energy through conversion of mechanical energy (e.g. through Kelvin-Helmholtz instabilities [33,43]). Although an exponential growth of the magnetic energy has been observed in local simulations [47,48], global simulations of binary NSs (i.e., like ours) have not yet reached the required accuracy to capture the dynamics occurring at the smallest scales. As a result, there is only moderate growth of the magnetic energy, which saturates at values lower than in local simulations.

Nevertheless, there are some useful qualitative observations from our simulations beyond the merger epoch. First, the magnetic flux through a hemisphere around the individual stars decreases after the merger; due to the reconnection of magnetic field lines, part of the ordered dipolar magnetosphere is ejected soon after the formation of the rotating hypermassive neutron star. As the stars lose their ordered dipolar magnetospheres and magnetic flux, the luminosity is expected to decrease (although this behavior might change due to the increase in the magnetic field strength at the merger). Notice however that, as discussed in [11], an ordered magnetosphere may emerge again at later times by dynamo action in a surface shear layer. Second, the luminosity of the U/u case grows even after merger until it becomes comparable to that of the other two cases. This growth is expected because the final configuration for all our cases is always an aligned rotator of the same rotational velocity and a magnetic dipole moment of comparable strength and extent.

We can also consider this system as if the stars were immersed in electrovacuum instead of being surrounded by tenuous plasma (i.e. magnetospheres). Recall that orbiting dipoles with equal, aligned moments produce no electromagnetic radiation at dipole order, while antialigned moments do (see Appendix A). Thus that the U/D case radiates more is not surprising. Nevertheless, such an argument resorting to electromagnetism would suggest that the U/u case should be more radiative than the U/U case because the effective dipole of the U/u is nonzero. However, in our calculations, it is instead the aligned case that is much more radiative, and the failure here indicates that this electrovacuum analogy can be taken only so far.

Another argument that ignores the magnetosphere suggests that the antialigned dipoles *liberate* potential energy as they get closer, whereas the aligned dipoles *require* the input of electromagnetic potential energy as they approach. One problem with this argument is that it would predict the radiation of the U/u case to fall between the other two, which is not the case.

It is interesting to point out here that in the U/u case the amount of energy dissipated as Joule heating $J_i E^i$ is comparable to the Poynting energy radiated. For the U/D and U/U cases, on the other hand, the energy dissipated as heat is only roughly a third of the radiated one. In summary, the Poynting integration indicates that magnetosphere interactions in the U/D and U/U cases yield additional radiation compared to, and with a different orbital dependence than, what could be explained via a simple unipolar induction model. This result is reinforced by the important differences in the Joule heat observed between the U/u case and the others.

V. OBSERVABILITY PROSPECTS

In this work we have studied the basic phenomenology of magnetosphere behavior of an inspiraling, magnetized binary neutron star system. Our results imply that the late orbiting stages of such a system can induce strong electromagnetic emissions, in addition to strong gravitational wave output. These electromagnetic emissions are sourced by the ability of the magnetosphere to tap rotational energy from the system and to induce both current sheets and Poynting flux. Interestingly, current sheets in the system are heterogeneous and have an imprint of the orbital behavior which could give time-varying signals that aid in detecting these systems electromagnetically. While a detailed analysis of these signatures is outside the scope of this work, we comment here on some possible relevant options.

A. Thermal spectra

The combination of very high energy density with a strong magnetic field as studied here is expected to

produce an optically thick environment emitting roughly as a blackbody (see Appendix B for a more detailed discussion). The effective temperature of this radiation can be calculated by balancing the Poynting luminosity (absorbed by the magnetospheric plasma) with the (blackbody) radiation emitted by the magnetosphere. Further, recall that the magnetic field will not affect the premerger dynamics provided that the strengths considered are $<10^{17}$ G. Therefore, the Poynting luminosities used to estimate the temperature can be rescaled as $\mathcal{L} \propto B^2$. We can then arrive at an expression for the temperature by extracting the total Poynting luminosity $\mathcal{L}$ emitted within a radius $r_o \approx 30$ km (i.e., around $t \approx -5$ ms) as

$$T = (10^7 \text{ K}) S_{AB} (B_{11})^{1/2} \tag{9}$$

where $B_{11} = B/10^{11}$ G and S_{AB} characterizes the configuration of the initial magnetic field. In particular, we find $S_{U/U} = 4.7$, $S_{U/u} = 2$, and $S_{U/D} = 10$ for the three cases studied here.

Notice that the luminosity in the U/u case obtained from our simulations has the same order of magnitude as the simple estimate obtained assuming the unipolar inductor model for the strongly magnetized star with a weakly magnetized companion in Eq. (3). This agreement leads to similar effective temperatures. From the effective temperature, computation of the peak frequency of the blackbody radiation [i.e., via Wien's displacement law $\nu_{\text{peak}} = (5.88 \times 10^{10} \text{ Hz/K}) T$], falls within the hard x-ray range. Notice that in the extreme case where the primary star (for the U/u case) is a magnetar with $B \sim 10^{15}$ G the luminosity will increase to $\mathcal{L}_{U/u} \approx 1.6 \times 10^{47}$ erg/s with a blackbody temperature $T_{U/u} = 2 \times 10^9$ K, well inside the γ-ray range.

B. Nonthermal components

Neutron stars and their magnetic configurations are responsible for a number of nonthermal emissions such as pulsars and soft gamma-ray repeaters, and clearly the systems studied here will have nonthermal emissions. One possibility, as argued in [30], is that the system's strong Poynting flux drives a relativistic bubble that pushes into the surrounding interstellar medium. At sufficiently large separations, the shock at the interface of the bubble becomes collisional and can be responsible for synchrotron radio emission. The details of the shock behavior however are more involved than those worked out in [30]. As our studies indicate, the Poynting flux is asymmetric and its complex time dependence is intimately tied to the initial field configuration of the stars.

As the orbit tightens, the shock would become collisionless and different processes would become important. In particular, the magnetic field far from the stars resembles that of the striped winds from pulsars. As shown in Fig. 15, the orbiting behavior induces an outflowing wind with regions of opposite magnetic field polarity similar to those

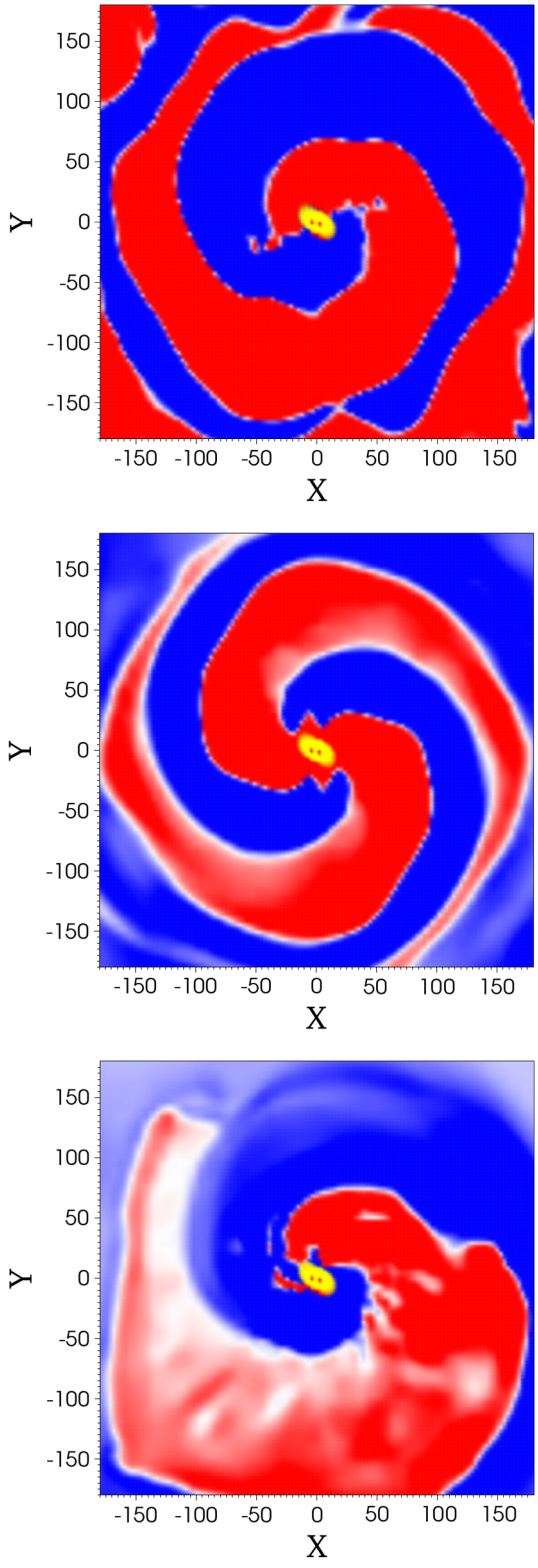

FIG. 15 (color online). Polarity (red positive, blue negative) of the B_z component of the magnetic field at $z = +7.4$ km above the orbital plane at late times ($t \approx 1.4$ ms; after the stars have already touched) for the U/D, U/U and U/u cases respectively. The pattern resembles a "striped" pattern. The density of the merging binary is also shown at the center of the figures.

discussed in the context of oblique rotators [49]. Models arguing for strong particle acceleration in pulsar winds [49] through shock-driven magnetic reconnections would consequently also be applicable here.

Furthermore, accelerating fields can arise naturally at gaps ([50–53]) energizing a population of particles that emit high energy, synchrotron radiation. Another emission mechanism as argued in e.g. [54,55] asserts that strong cooling at the current sheets, such as we see in the U/U and U/D cases, can give rise to gamma rays via synchrotron radiation [55] or inverse Compton scattering (see for instance [56]). Flares of intense gamma rays at the radiation-reaction limit have been observed from the Crab Nebula but without significantly detected components in the rest of the electromagnetic spectrum [57,58]. These observations perhaps implicate regions of magnetic reconnection as sites of tremendous particle acceleration. Here we are in a situation with a very dynamic magnetic configuration and favorable sites for particle acceleration likely arise.

VI. FINAL WORDS

We have shown that global magnetic fields within a binary system can give rise to a rich phenomenology that powers strong emissions on the electromagnetic side [$\simeq 10^{40-43}(B/10^{11}\ \mathrm{G})^2$ erg/s] prior to the merger. These luminosities are at the level of the brightest pulsars and beyond and would bear particular characteristics tied to the orbital behavior. Such high luminosities, together with the power emitted in gravitational waves, indicate that the system is strongly radiative in multiple bands and channels. We have also identified possible features that can lead to observable signals tied to the orbital behavior of the system. The consequential time-dependent nature of possible emissions might help in their detection, especially if some prior localization (in time and space) is provided by gravitational wave information. The details of the emission mechanism however are still uncertain. Different emission mechanisms are expected near the current sheets, where strong cooling can give rise to gamma rays [54,55] produced via either synchrotron [55] or inverse Compton scattering [56] (see also discussion in [59]). Also, at gaps, accelerating fields can develop [50–53] and energize particles which could also emit at high energies via curvature and synchrotron radiation. Understanding which of these mechanisms are the most relevant is yet unknown even in pulsar models so there is a large degree of uncertainty in this question. At a simple level however, a relativistically expanding electron-positron wind sourced by energy dissipation and magnetohydrodynamical waves in between the stars could create an x-ray signature [8] preceding or coincident with the merger. Thus, ISS-Lobster [60] with its high sensitivity and wide field of view would be very well suited for detecting the associated electromagnetic counterpart to a binary neutron star merger. For the values calculated here these sources would be observable to distances of $10^{0-2}(B/10^{11}\ \mathrm{G})$ Mpc (assuming 10% efficient conversion of Poynting flux).

ACKNOWLEDGMENTS

It is a pleasure to thank A. Broderick, J. McKinney, A. Spitkovksy and C. Thompson for interesting discussions. This work was supported by the NSF under Grants No. PHY-0969827 (LIU) and No. PHY-0969811 (BYU), NASA's ATP program through Grant No. NNX13AH01G, NSERC through a Discovery Grant (to LL) and CIFAR (to LL). C. P. acknowledges support by the Jeffrey L. Bishop Fellowship. Research at Perimeter Institute is supported through Industry Canada and by the Province of Ontario through the Ministry of Research & Innovation. Computations were performed at XSEDE and Scinet.

APPENDIX A: ELECTROVACUUM CALCULATION OF RADIATION

The radiated electromagnetic energy of two dipoles in electrovacuum can be obtained via the post-Newtonian equations of motion. The rate of energy loss due to electromagnetic radiation to 2.5 PN order (which includes gravitational radiation effects) has been presented in [39,61] under the assumption that the stars' magnetic dipoles remain constant and, neglecting spin-orbit effects,

$$\frac{dE}{dt} = -\frac{2}{15}\frac{m^2}{r^6}[2\mu_{\mathrm{eff}}^2\{v^2 - 6\dot{r}(\hat{n}\cdot\vec{v}) + 9\dot{r}^2\} - \{\vec{\mu}_{\mathrm{eff}}\cdot(\vec{v} - 2\dot{r}\,\hat{n})\}^2] \tag{A1}$$

where $r = |\vec{r}_2 - \vec{r}_1|$ is the separation between the stars, $\vec{v} = \vec{v}_2 - \vec{v}_1$ is the relative velocity, and $\hat{n} = \vec{r}/r$ represents the unit vector between the stars in the center of mass frame; $m = m_1 + m_2$ is the total mass of the system; and $\vec{\mu}_{\mathrm{eff}} = (m_2\vec{\mu}_{(1)} - m_1\vec{\mu}_{(2)})/m$ represents the effective magnetic dipole of the system. In the case of an equal mass binary system with identical magnetic dipoles (i.e. same direction and magnitude; U/U) $\vec{\mu}_{\mathrm{eff}} = 0$ and no radiation is produced at this order. On the other hand, the choice of antialigned moments (U/D) maximizes the predicted radiation.

Moreover, assuming a circular orbit with $\dot{r} = 0$, an effective magnetic dipole moment perpendicular to the velocity, and a Keplerian rotational frequency Ω, it is straightforward to determine that the radiated energy scales as $\Omega^{14/3}$, at leading order. Notice that this scaling is the same as in Eq. (4), the estimate provided by the unipolar inductor model for the U/u case, although its magnitude in the electrovacuum case is a few orders of magnitude smaller than in the force-free case.

APPENDIX B: RELATIVISTIC OUTFLOW AND BLACKBODY RADIATION

As has been noted in [54], the release of electromagnetic energy with sufficiently high energy density will produce a relativistic outflow of electron-positron pair plasma with a roughly blackbody spectrum as long as the medium is optically thick. Such a condition is naturally induced by a magnetic field with strength on the order of the quantum critical field $B_{\rm QED} = 4.4 \times 10^{13}$ G. At this strength, the magnetic energy density is high enough for copious pair production, and the resulting medium becomes optically thick due to electron scattering and pair production. In this regime, the radiated energy will produce a relativistic wind of radiation and pairs [62].

To estimate the effective temperature we can proceed as follows. First, let us define the normalized temperature $\Theta_e \equiv k_B T/(m_e c^2)$ and the normalized magnetic field $b \equiv B/B_{\rm QED}$ and recall that pair production can lead to an optically thick regime (for which it is safe to assume approximate blackbody radiation). In such a regime, we can assume that in equilibrium the electromagnetic energy injection must equal the total pressure leading to the pressure-balance relation

$$P_{\rm rad} + P_{\rm pairs} + P_{\rm baryon} = \frac{(bB_{\rm QED})^2}{8\pi} \tag{B1}$$

where $P_{\rm rad}$, $P_{\rm pairs}$, $P_{\rm baryon}$ are the pressures associated with photons, electron-positron pairs, and baryons respectively. Next, we set $P_{\rm rad} = aT^4/3$ and assume that the baryon pressure of the charge density is small. Furthermore, we note that the resulting pressure of electron-positron pairs in thermal equilibrium is negligible for $\Theta_e \ll 1$, while for $\Theta_e \geq 1$ it is comparable to the radiation pressure $P_{\rm pairs} = 7P_{\rm rad}/4$ [54]. Combining these assumptions with Eq. (B1) yields

$$\Theta_e \sim \kappa b^{1/2} \tag{B2}$$

where κ is just a numerical coefficient equal either to 2.2 for $\Theta_e \ll 1$ or 1.7 for $\Theta_e \geq 1$. In the following we consider an intermediate value $\Theta_e \sim 2b^{1/2}$ which will be roughly valid for any temperature.

Now, as discussed for large magnetic fields $b > 1$ (i.e., corresponding to high effective temperatures $\Theta_e \geq 1$) a dense pair plasma is easily produced and the medium is optically thick. For low temperatures, $\Theta_e < 1$, the density of pairs is $n_\pm = (4.4 \times 10^{30}\ {\rm cm}^{-3})\Theta_e^{3/2} e^{-1/\Theta_e}$, leading to an opacity $\kappa \sim (\sigma_T n_\pm) \sim (2.9 \times 10^6\ {\rm cm}^{-1})\Theta_e^{3/2} e^{-1/\Theta_e}$. Taking, for instance, a realistic magnetic field value of $B \sim 4 \times 10^{11}$ G yields a normalized temperature of $\Theta_e \sim 0.2$. This choice also gives an optical depth $\lambda \sim \kappa^{-1} \simeq 6 \times 10^{-4}$ cm and a characteristic diffusion time $\tau_{\rm diff} \sim R^2/(\lambda c)$ (in terms of some characteristic length scale R). A lower bound for $\tau_{\rm diff}$ is obtained by choosing $R \sim 10^6$ cm (commensurate with a typical NS radius) with $\tau_{\rm diff} \geq 6 \times 10^4$ s.

These arguments suggest that even for more moderate field strengths below $B_{\rm QED}$ but above $\simeq 10^{11}$ G, the system will become optically thick to photons and radiate with a blackbody spectrum. The characteristic temperature of the radiation can be determined by equating the blackbody power given by the Stefan-Boltzmann law with the sum of the Poynting flux and dissipated power

$$\sigma_{\rm SB} T^4 \sim S_{\rm Poynting} + S_{\rm diss} \sim \frac{\mathcal{L}}{4\pi r_o^2}. \tag{B3}$$

Here, $\mathcal{L}$ is the total power radiated either as Poynting flux or dissipated at the shear layer, with r_o the characteristic radius where most of this energy is injected. Using Eq. (3), setting $r_o = a$, and assuming that the dissipated energy at shear layers is a small fraction of the Poynting flux, we obtain

$$\sigma_{\rm SB} T^4 \sim (1.5 \times 10^{26}\ {\rm ergs/(cm^2\,s)}) \left(\frac{B_*}{10^{11}\ {\rm G}}\right)^2 \left(\frac{a}{30\ {\rm km}}\right)^{-9} \tag{B4}$$

leading to a very high effective temperature

$$T \sim (4 \times 10^7\ {\rm K}) \left(\frac{B_*}{10^{11}\ {\rm G}}\right)^{1/2} \left(\frac{a}{30\ {\rm km}}\right)^{-9/4}. \tag{B5}$$

However, as mentioned, the applicability of this estimate depends strongly on the magnetic field behavior and so on the stage at which it can be adopted.

[1] E. Nakar, Phys. Rep. **442**, 166 (2007).
[2] E. Troja, S. Rosswog, and N. Gehrels, Astrophys. J. **723**, 1711 (2010).
[3] L. Z. Kelley, I. Mandel, and E. Ramirez-Ruiz, Phys. Rev. D **87**, 123004 (2013).
[4] K. Kyutoku, K. Ioka, and M. Shibata, arXiv:1209.5747.
[5] D. Tsang, J. S. Read, T. Hinderer, A. L. Piro, and R. Bondarescu, Phys. Rev. Lett. **108**, 011102 (2012).
[6] A. L. Piro, Astrophys. J. **755**, 80 (2012).
[7] D. Lai, Astrophys. J. **757**, L3 (2012).
[8] B. M. S. Hansen and M. Lyutikov, Mon. Not. R. Astron. Soc. **322**, 695 (2001).
[9] M. Vietri, Astrophys. J. **471**, L95 (1996).
[10] V. M. Lipunov and I. E. Panchenko, Astron. Astrophys. **312**, 937 (1996).
[11] L. Lehner, C. Palenzuela, S. L. Liebling, C. Thompson, and C. Hanna, Phys. Rev. D **86**, 104035 (2012).

[12] C. Palenzuela, L. Lehner, M. Ponce, S. L. Liebling, M. Anderson, D. Neilsen, and P. Motl, Phys. Rev. Lett. **111**, 061105 (2013).

[13] C. Palenzuela, Mon. Not. R. Astron. Soc. **431**, 1853 (2013).

[14] C. Palenzuela, L. Lehner, O. Reula, and L. Rezzolla, Mon. Not. R. Astron. Soc. **394**, 1727 (2009).

[15] K. Dionysopoulou, D. Alic, C. Palenzuela, L. Rezzolla, and B. Giacomazzo, Phys. Rev. D **88**, 044020 (2013).

[16] T. W. Baumgarte and S. L. Shapiro, Phys. Rev. D **59**, 024007 (1998).

[17] M. Shibata and T. Nakamura, Phys. Rev. D **52**, 5428 (1995).

[18] D. Neilsen, L. Lehner, C. Palenzuela, E. W. Hirschmann, S. L. Liebling, P. M. Motl, and T. Garrett, Proc. Natl. Acad. Sci. U.S.A. **108**, 12641 (2011).

[19] G. Calabrese, L. Lehner, D. Neilsen, J. Pullin, O. Reula, O. Sarbach, and M. Tiglio, Classical Quantum Gravity **20**, L245 (2003).

[20] G. Calabrese, L. Lehner, O. Reula, O. Sarbach, and M. Tiglio, Classical Quantum Gravity **21**, 5735 (2004).

[21] M. Anderson, E. Hirschmann, S. L. Liebling, and D. Neilsen, Classical Quantum Gravity **23**, 6503 (2006).

[22] M. Anderson, E. Hirschmann, L. Lehner, S. L. Liebling, P. Motl, D. Neilsen, C. Palenzuela, and J. Tohline, Phys. Rev. D **77**, 024006 (2008).

[23] HAD home page, http://had.liu.edu.

[24] S. L. Liebling, Phys. Rev. D **66**, 041703 (2002).

[25] L. Lehner, S. L. Liebling, and O. Reula, Classical Quantum Gravity **23**, S421 (2006).

[26] F. Pretorius, Ph.D. thesis, The University of British Columbia, 2002.

[27] M. Branchesi, A. Klotz, and M. Laas-Bourez (LIGO Scientific Collaboration, Virgo Collaboration), arXiv:1110.3169.

[28] B. Sathyaprakash and B. F. Schutz, Living Rev. Relativity **12**, 2 (2009), http://www.livingreviews.org/lrr-2009-2.

[29] J. S. Bloom, D. E. Holz, S. A. Hughes, K. Menou, A. Adams *et al.*, arXiv:0902.1527.

[30] M. V. Medvedev and A. Loeb, arXiv:1212.0333.

[31] A. Buonanno, L. E. Kidder, and L. Lehner, Phys. Rev. D **77**, 026004 (2008).

[32] L. Baiotti, T. Damour, B. Giacomazzo, A. Nagar, and L. Rezzolla, Phys. Rev. D **84**, 024017 (2011).

[33] M. Anderson, E. W. Hirschmann, L. Lehner, S. L. Liebling, P. M. Motl, D. Neilsen, C. Palenzuela, and J. E. Tohline, Phys. Rev. Lett. **100**, 191101 (2008).

[34] Y. T. Liu, S. L. Shapiro, Z. B. Etienne, and K. Taniguchi, Phys. Rev. D **78**, 024012 (2008).

[35] B. Giacomazzo, L. Rezzolla, and L. Baiotti, Mon. Not. R. Astron. Soc. **399**, L164 (2009).

[36] L. Rezzolla, B. Giacomazzo, L. Baiotti, J. Granot, C. Kouveliotou, and M. A. Aloy, Astrophys. J. **732**, L6 (2011).

[37] J. S. Read, C. Markakis, M. Shibata, K. Uryu, J. D. Creighton, M. Shibata, K. Uryū, J. Creighton, and J. Friedman, Phys. Rev. D **79**, 124033 (2009).

[38] T. Damour, A. Nagar, and L. Villain, Phys. Rev. D **85**, 123007 (2012).

[39] K. Ioka and K. Taniguchi, Astrophys. J. **537**, 327 (2000).

[40] LORENE home page, http://www.lorene.obspm.fr/.

[41] M. Burgay, N. D'Amico, A. Possenti, R. N. Manchester, A. G. Lyne, B. C. Joshi, M. A. McLaughlin, M. Kramer, J. M. Sarkissian, F. Camilo, V. Kalogera, C. Kim, and D. R. Lorimer, Nature (London) **426**, 531 (2003).

[42] F. A. Jenet and S. M. Ransom, Nature (London) **428**, 919 (2004).

[43] D. J. Price and S. Rosswog, Science **312**, 719 (2006).

[44] M. Obergaulinger, M. A. Aloy, and E. Muller, arXiv:1003.6031.

[45] A. Spitkovsky, Astrophys. J. **648**, L51 (2006).

[46] A. Tchekhovskoy and A. Spitkovsky, arXiv:1211.2803 [Mon. Not. R. Astron. Soc. (to be published)].

[47] W. Zhang, A. MacFadyen, and P. Wang, Astrophys. J. **692**, L40 (2009).

[48] M. Obergaulinger, M. A. Aloy, and E. Müller, Astron. Astrophys. **515**, A30 (2010).

[49] L. Sironi and A. Spitkovsky, Astrophys. J. **741**, 39 (2011).

[50] R. W. Romani and I.-A. Yadigaroglu, Astrophys. J. **438**, 314 (1995).

[51] K. S. Cheng, M. Ruderman, and L. Zhang, Astrophys. J. **537**, 964 (2000).

[52] A. G. Muslimov and A. K. Harding, Astrophys. J. **588**, 430 (2003).

[53] A. G. Muslimov and A. K. Harding, Astrophys. J. **606**, 1143 (2004).

[54] D. A. Uzdensky, Space Sci. Rev. **160**, 45 (2011).

[55] D. A. Uzdensky and A. Spitkovsky, arXiv:1210.3346.

[56] M. Lyutikov, arXiv:1208.5329.

[57] R. Buehler *et al.*, Astrophys. J. **749**, 26 (2012).

[58] M. C. Weisskopf *et al.*, Astrophys. J. **765**, 56 (2013).

[59] J. Arons, Astron. Astrophys. Suppl. Ser. **120**, C49 (1996).

[60] J. Camp, S. D. Barthelmy, L. Blackburn, K. Carpenter, N. Gehrels *et al.*, arXiv:1304.3705.

[61] L. Blanchet, Living Rev. Relativity **5**, 3 (2002).

[62] B. Paczynski, Astrophys. J. Lett. **308**, L43 (1986).